

Le Luo^{1,2} · J. E. Thomas^{1,3}

Thermodynamic Measurements in a Strongly Interacting Fermi Gas

11.4.2008

Keywords Fermi gas, strong interactions, thermodynamics, superfluidity, phase transition, critical parameters

Abstract Strongly interacting Fermi gases provide a clean and controllable laboratory system for modeling strong interparticle interactions between fermions in nature, from high temperature superconductors to neutron matter and quark-gluon plasmas. Model-independent thermodynamic measurements, which do not require theoretical models for calibrations, are very important for exploring this important system experimentally, as they enable direct tests of predictions based on the best current non-perturbative many-body theories. At Duke University, we use all-optical methods to produce a strongly interacting Fermi gas of spin-1/2-up and spin-1/2-down ^6Li atoms that is magnetically tuned near a collisional (Feshbach) resonance. We conduct a series of measurements on the thermodynamic properties of this unique quantum gas, including the energy E , entropy S , and sound velocity c . Our model-independent measurements of E and S enable a precision study of the finite temperature thermodynamics. The $E(S)$ data are directly compared to several recent predictions. The temperature in both the superfluid and normal fluid regime is obtained from the fundamental thermodynamic relation $T = \partial E / \partial S$ by parameterizing the $E(S)$ data using two different power laws that are joined with continuous E and T at a certain entropy S_c , where the fit is optimized. We observe a significant change in the scaling of E with S above and below S_c . Taking the fitted value of S_c as an estimate of the critical entropy for a superfluid-normal fluid phase transition in the strongly interacting Fermi gas, we estimate the critical parameters. Our $E(S)$ data are also used to experimentally calibrate the endpoint temperatures obtained for adiabatic sweeps of the magnetic field between the ideal and strongly interacting regimes. This enables the first experimental calibration of the temperature scale used in experiments on fermionic pair condensation, where

1: Department of Physics, Duke University, Durham, NC 27708

2: Current address: Joint Quantum Institute, University of Maryland and National Institute of Standards and Technology, College Park, MD 20742

3: E-mail: jet@phy.duke.edu

the ideal Fermi gas temperature is measured before sweeping the magnetic field to the strongly interacting regime. Our calibration shows that the ideal gas temperature measured for the onset of pair condensation corresponds closely to the critical temperature T_c estimated in the strongly interacting regime from the fits to our $E(S)$ data. We also calibrate the empirical temperature employed in studies of the heat capacity and obtain nearly the same T_c . We determine the ground state energy by three different methods, using sound velocity measurements, by extrapolating $E(S)$ to $S = 0$ and by measuring the ratio of the cloud sizes in the strongly and weakly interacting regimes. The results are in very good agreement with recent predictions. Finally, using universal thermodynamic relations, we estimate the chemical potential and heat capacity of the trapped gas from the $E(S)$ data.

PACS numbers: 03.75.Ss

1 Introduction

Interacting fermionic particles play a central role in the structure of matter and exist over a very broad range of energies, from extremely low temperature trapped atomic Fermi gases, where $T < 10^{-7}$ K^{1,2}, to very high temperature primordial matter, like quark-gluon plasmas, where $T > 10^{12}$ K³. For all of these systems, the most intriguing physics is related to very strong interactions between fermionic particles, such as the strong coupling between electrons in high- T_c superconductors and the strong interactions between neutrons in neutron matter.

Current many-body quantum theories face great challenges in solving problems for strongly interacting Fermi systems, due to the lack of a small coupling parameter. For example, the critical temperature of a superfluid-normal fluid transition in a strongly interacting Fermi gas has been controversial for many years. The critical temperature T_c/T_F has been predicted to have values in the range between 0.15 and 0.35 by different theoretical methods^{4,5,6,7,8,9,10,11}. A complete understanding of the physics of strongly interacting systems can not yet be obtained from a theoretical point of view. There is a pressing need to investigate strongly interacting fermions experimentally.

In recent years, based on progress in optical cooling and trapping of fermionic atoms, a clean and controllable strongly interacting Fermi system, comprising a degenerate, strongly interacting Fermi gas^{1,2}, is now of interest to the whole physics community. Strongly interacting Fermi gases are produced near a broad Feshbach resonance^{1,12,13}, where the zero energy s-wave scattering length a_s is large compared to the interparticle spacing, while the interparticle spacing is large compared to the range of the two-body interaction. In this regime, the system is known as a unitary Fermi gas, where the properties are universal and independent of the details of the two-body scattering interaction^{14,15}. In contrast to other strongly interacting Fermi systems, in atomic gases, the interactions, energy, and spin population can be precisely adjusted, enabling a variety of experiments for exploring this model system.

Intense studies of strongly interacting Fermi gases have been implemented over the past several years from a variety of perspectives. Some of the first experiments observed the expansion hydrodynamics of the strongly interacting cloud^{1,16}.

Evidence for superfluid hydrodynamics was first observed in collective modes^{17,18}. Collective modes were later used to study the $T = 0$ equation of state throughout the crossover regime^{19,20,21}. Recently, measurements of sound velocity have also been used to explore the $T = 0$ equation of state²². Below a Feshbach resonance, fermionic atoms join to form stable molecules and molecular Bose-Einstein condensates^{23,24,25,26,27}. Fermionic pair condensation has been observed by projection experiments using fast magnetic field sweeps^{26,27}. Above resonance, strongly bound pairs have been probed by radio frequency and optical spectroscopy^{28,29,30,31}. Phase separation has been observed in spin polarized samples^{32,33}. Rotating Fermi gases have revealed vortex lattices in the superfluid regime^{34,35} as well as irrotational flow in both the superfluid and normal fluid regimes³⁶. Measurement of the thermodynamic properties of a strongly interacting Fermi gas was first accomplished by adding a known energy to the gas, and then determining an empirical temperature that was calibrated using a pseudogap theory³⁷. Recent model-independent measurements of the energy and entropy³⁸ provide a very important piece of the puzzle, because they enable direct and precision tests that distinguish predictions from recent many-body theories, without invoking any specific theoretical model^{4,5}.

One of the major challenges for the experiments in strongly interacting Fermi gases is the lack of a precise model-independent thermometry. Two widely-used thermometry methods are model-dependent, in that they rely on theoretical models for calibration. The first relies on adiabatic magnetic field sweeps between the molecular BEC regime and the strongly interacting regime^{28,39}. Subsequently, the temperature of the strongly interacting gas is estimated from the measured temperature in the BEC regime using a theoretical model of the entropy⁸. The second method, used by our group³⁷, is based on determining an empirical temperature from the cloud profiles that is calibrated by comparing the measured density distribution with a theoretical model for the density profiles. Currently two model-independent thermometry methods have been reported for strongly-interacting gases. One is the technique employed by the MIT group⁴⁰, which is only applicable to imbalanced mixtures of spin-up and spin-down atoms. That method is based on fitting the noninteracting edge for the majority spin after phase separation. Another model-independent method is demonstrated in Ref.³⁸, which is applicable to both balanced and imbalanced mixtures of spin-up and spin-down fermions. The energy E and entropy S are measured and then parameterized to determine a smooth curve $E(S)$. Then the temperature in both the superfluid and normal fluid regime is obtained from the fundamental thermodynamic relation $T = \partial E / \partial S$.

In this paper, we will describe our model-independent thermodynamic experiments on a strongly interacting Fermi gas of ^6Li , which we have conducted at Duke University. First, we will describe our measurements of both the total energy E and the total entropy S of a trapped strongly-interacting Fermi gas tuned near a Feshbach resonance. Then, we determine the temperature $T = \partial E / \partial S$ after showing that the $E(S)$ data are very well parameterized by using two different power laws that are joined with continuous E and T at a certain entropy S_c that gives the best fit. To examine the sensitivity of the temperature to the form of the fit function, we employ two different fit functions that allow for a heat capacity jump or for a continuous heat capacity at S_c . We find that the T values closely agree for both cases. We find a significant change in the scaling of E with S above

and below S_c , in contrast to the behavior for an ideal Fermi gas, where a single power-law well parameterizes $E(S)$ over the same energy range. By interpreting S_c as the critical entropy for a superfluid-normal fluid transition in the strongly interacting Fermi gas, we estimate the critical energy E_c and critical temperature T_c . Both the model-independent $E(S)$ data and the estimated critical parameters are compared with several recent many-body theories based on both analytic and quantum Monte Carlo methods.

We also show how parameterizing the $E(S)$ data provides experimental temperature calibrations, which helps to unify, in a model-independent way, the results obtained by several groups^{26,27,31,37,38}. First we relate the endpoint temperatures for adiabatic sweeps of the bias magnetic field between the strongly interacting and ideal noninteracting regimes, as used in the JILA experiments to characterize the condensed pair fraction^{26,31}. This enables the ideal gas temperature observed for the onset of pair condensation^{26,31} to be related to the critical temperature of the strongly interacting Fermi gas. The temperature obtained by parameterizing the strongly interacting gas data also calibrates the empirical temperature based on the cloud profiles, as used in our previous studies of the heat capacity³⁷. These temperature calibrations yield values of T_c close to that estimated from our $E(S)$ data.

Next, we discuss three different methods for determining the universal many-body parameter, β^{-1} , where $1 + \beta$ is the energy per particle in a uniform strongly interacting Fermi gas at $T = 0$ in units of the energy per particle of an ideal Fermi gas at the same density. First, we describe the measurement of the sound velocity at resonance and its relationship to β . Then, we determine β from the ground state energy E_0 of the trapped gas. Here, E_0 is obtained by extrapolating the $E(S)$ data to $S = 0$, as suggested by Hu et al.⁴. This avoids a systematic error in the sound velocity experiments arising from the unknown finite temperature. Finally, to explore the systematic error arising from the measurement of the number of atoms, β is determined in a number-independent manner from the ratio of the cloud sizes in the strongly and weakly interacting regimes. All three results are found to be in very good agreement with each other and with recent predictions.

Finally, we obtain three universal thermodynamic functions from the parameterized $E(S)$ data, the energy $E(T)$, heat capacity $C(T)$, and global chemical potential $\mu_g(E)$.

2 Experimental Methods

Our experiments begin with an optically-trapped highly degenerate, strongly interacting Fermi gas of $^6\text{Li}^1$. A 50:50 mixture of the two lowest hyperfine states of ^6Li atoms is confined in an ultrastable CO_2 laser trap with a bias magnetic field of 840 G, just above a broad Feshbach resonance at $B = 834 \text{ G}^{41}$. At 840 G, the gas is cooled close to the ground state by lowering the trap depth $U^{1,13}$. Then U is recompressed to a final trap depth of $U_0/k_B = 10 \mu\text{K}$, which is much larger than the energy per particle of the gas, for the highest energies employed in the experiments. This suppresses evaporation during the time scale of the measurements. The shallow trap yields a low density that suppresses three body loss and heating. The low density also yields a weakly interacting sample when the bias

magnetic field is swept to 1200 G, although the scattering length is -2900 bohr, as discussed in detail in § 2.2.

The shape of the trapping potential is that of a gaussian laser beam, with a transverse gaussian profile determined by the spot size and an axial lorentzian profile determined by the Rayleigh length. To simplify the calculations of the ideal gas properties in subsequent sections, as well as the theoretical modelling, we take the trap potential to be approximated by a three dimensional gaussian profile,

$$U(x, y, z) = U_0 \left(1 - \exp \left(-\frac{2x^2}{a_x^2} - \frac{2y^2}{a_y^2} - \frac{2z^2}{a_z^2} \right) \right), \quad (1)$$

where $a_{x,y,z}$ is the $1/e^2$ width of trap for each direction. Here, we take the zero of energy to be at $\mathbf{r} = 0$. When the cold atoms stay in the deepest portion of the optical trap, where $x(y, z) \ll a_x(a_y, a_z)$, the gaussian potential can be well approximated as a harmonic trap with transverse frequencies ω_x , ω_y and axial frequency ω_z , where

$$\omega_{x,y,z} = \sqrt{\frac{4U_0}{ma_{x,y,z}^2}}. \quad (2)$$

Here m is the ${}^6\text{Li}$ mass. At our final trap depth U_0 , the measured transverse frequencies are $\omega_x = 2\pi \times 665(2)$ Hz and $\omega_y = 2\pi \times 764(2)$ Hz. The axial frequency is weakly magnetic field dependent since the total axial frequency has both an optical potential contribution ω_{oz}^2 determined by Eq. 2 and a magnetic potential contribution arising from magnetic field curvature, ω_{mz}^2 . The net axial frequency is then $\omega_z = \sqrt{\omega_{oz}^2 + \omega_{mz}^2}$. We find $\omega_z = 2\pi \times 30.1(0.1)$ Hz at 840 G and $\omega_z = 2\pi \times 33.2(0.1)$ Hz at 1200 G. The total number of atoms is $N \simeq 1.3 \times 10^5$. The corresponding Fermi energy E_F and Fermi temperature T_F at the trap center for an ideal noninteracting harmonically trapped gas are $E_F = k_B T_F \equiv \hbar \bar{\omega} (3N)^{1/3}$, where $\bar{\omega} = (\omega_x \omega_y \omega_z)^{1/3}$. For our trap conditions, we obtain $T_F \simeq 1.0 \mu\text{K}$.

Using $\bar{\omega}$, we can rewrite Eq. 1 as a symmetric effective potential,

$$U(\mathbf{r}) = U_0 \left(1 - \exp \left(-\frac{m\bar{\omega}^2 \mathbf{r}^2}{2U_0} \right) \right), \quad (3)$$

where \mathbf{r} is the scaled position vector. Here, $\mathbf{r}^2 = \tilde{x}^2 + \tilde{y}^2 + \tilde{z}^2$ with $\tilde{x} = \omega_x x / \bar{\omega}$, $\tilde{y} = \omega_y y / \bar{\omega}$, $\tilde{z} = \omega_z z / \bar{\omega}$. To obtain the anharmonic corrections for the gaussian trap, we expand Eq. 3 in a Taylor series up to second order in \mathbf{r}^2 ,

$$U(\mathbf{r}) = \frac{m\bar{\omega}^2 \mathbf{r}^2}{2} - \frac{m^2 \bar{\omega}^4 \mathbf{r}^4}{8U_0}. \quad (4)$$

2.1 Energy Measurement

Model-independent energy measurement is based on a virial theorem, which for an ideal gas in a harmonic confining potential U_{ho} yields $E = 2\langle U_{ho} \rangle$. Since the

harmonic potential energy is proportional to the mean square cloud size, measurement of the cloud profile determines the total energy. Remarkably, a trapped unitary Fermi gas at a broad Feshbach resonance obeys the same virial theorem as an ideal gas, although it contains superfluid pairs, noncondensed pairs, and unpaired atoms, all strongly interacting. This has been demonstrated both theoretically and experimentally⁴². The virial theorem shows that the total energy of the gas at all temperatures can be measured from the cloud profile using

$$E = \left\langle U + \frac{1}{2} \mathbf{x} \cdot \nabla U \right\rangle, \quad (5)$$

where U is the trapping potential and \mathbf{x} is the position vector. Eq. 5 can be shown to be valid for any trapping potential U and for any spin mixture, without assuming either the local density approximation or harmonic confinement^{43,44,45,46}.

Using Eq. 4 in Eq. 5 and keeping the lowest order anharmonic corrections, we obtain the energy per atom in terms of the axial mean square size,

$$E = 3m\omega_z^2 \langle z^2 \rangle \left[1 - \frac{5}{8} \frac{m\omega_z^2 \langle z^4 \rangle}{U_0 \langle z^2 \rangle} \right]. \quad (6)$$

Here, we have used the local density approximation with a scalar pressure, which ensures that $\langle x \partial U / \partial x \rangle = \langle y \partial U / \partial y \rangle = \langle z \partial U / \partial z \rangle$. For the ground state, where the spatial profile is a zero temperature Thomas-Fermi profile, we have $\langle z^4 \rangle = 12 \langle z^2 \rangle^2 / 5$. For energies $E/E_F > 1$, where the spatial profile is approximately gaussian, we have $\langle z^4 \rangle = 3 \langle z^2 \rangle^2$. Since the anharmonic correction is small at low temperatures where the cloud size is small, we use the gaussian approximation over the whole range of energies explored in our experiments. For the conditions of our experiments, there is no evidence that the local density approximation breaks down for a 50:50 spin mixture. In this case, measurement of the mean square size in any one direction determines the total energy. From Eq. 6, we see that by simply measuring the axial mean square size $\langle z^2 \rangle_{840}$ at 840 G and measuring the axial trap frequency by parametric resonance, we actually measure E_{840} , the total energy per particle of the strongly interacting Fermi gas at 840 G. This determines the total energy per particle in a model-independent way³⁸.

2.2 Entropy Measurement

The entropy S of the strongly interacting gas at 840 G is determined by adiabatically sweeping the bias magnetic field from 840 G to 1200 G, where the gas is weakly interacting³⁸. The entropy S_W of the weakly interacting gas is essentially the entropy of an ideal Fermi gas in a harmonic trap, which can be calculated in terms of the mean square axial cloud size $\langle z^2 \rangle_{1200}$ measured after the sweep. Since the sweep is adiabatic, we have

$$S = S_W. \quad (7)$$

The adiabaticity of the magnetic field sweep is verified by employing a round-trip-sweep: The mean square size of the cloud at 840 G after a round-trip-sweep lasting 2s is found to be within 3% of mean square size of a cloud that remains at

840 G for a hold time of 2s. The nearly unchanged atom number and mean square size proves the sweep does not cause any significant atom loss or heating, which ensures entropy conservation for the sweep. The background heating rate is the same with and without the sweep and increases the mean square size by about 2% over 2s. The mean square size data are corrected by subtracting the increase arising from background heating over the 1 s sweep time³⁸.

At 1200 G in our shallow trap, we have $k_F a_S = -0.75$, where the Fermi wavevector $k_F = (2mE_F/\hbar^2)^{1/2}$ and the s-wave scattering length $a_S = -2900$ bohr⁴¹. We find that the gas is weakly interacting: For the lowest temperatures attained in our experiments, the gas at 1200 G is a normal fluid that we observe to expand ballistically. We have calculated the ground state mean square size at 1200 G in our gaussian trap, based on a mean-field theory, $\langle z^2 \rangle_{W0} = 0.69 z_F^2(1200G)$ ³⁸, which is close to that of an ideal harmonically trapped gas, $\langle z^2 \rangle_{I0} = 0.75 z_F^2(1200G)$. Here, $z_F^2(B)$ is the mean square size corresponding to the Fermi energy of an ideal noninteracting Fermi gas at magnetic field B , which includes the magnetic field dependence of the axial trapping frequency: $E_F(B) \equiv 3m\omega_z^2(B)z_F^2(B)$.

We expect that the entropy of the gas at 1200 G is close to that of an ideal gas, except for a mean field shift of the energy. We therefore assume that a reasonable approximation to the entropy is that of an ideal Fermi gas, $S_I(\langle z^2 \rangle_I - \langle z^2 \rangle_{I0})$, where $\langle z^2 \rangle_{I0}$ is the ground state mean square size of an ideal Fermi gas in the gaussian trapping potential of Eq. 3. Here, we apply an elementary calculation based on integrating the density of states for the gaussian trap with the entropy per orbital $s = -k_B[f \ln f + (1-f) \ln(1-f)]$, where $f(\epsilon)$ is the ideal Fermi gas occupation number at temperature T for an orbital of energy ϵ . By calculating S_I as a function of the *difference* between the finite temperature and ground state mean square cloud sizes, we reduce the error arising from the mean field shift at 1200 G, and ensure that $S_I = 0$ for the ground state.

The exact entropy of a weakly interacting gas S_W at 1200G, $S_W(\langle z^2 \rangle_W - \langle z^2 \rangle_{W0})$, has been calculated using many-body theories^{4,7} for the gaussian potential of Eq. 3. In the experiments, we determine the value of $\langle z^2 \rangle_W - \langle z^2 \rangle_{W0}$, where we take $\langle z^2 \rangle_{W0} = 0.71 z_F^2(1200)$, the value measured at our lowest energy at 1200 G by extrapolation to $T = 0$ using the Sommerfeld expansion for the spatial profile of an ideal gas. This result is close to the theoretical value, $0.69 z_F^2(1200)$.

The entropy versus cloud size curve for an ideal noninteracting Fermi gas and the exact value for a weakly interacting gas S_W at 1200 G are plotted in Fig. 1. We find that the entropies $S_W(\Delta \langle z^2 \rangle = \langle z^2 \rangle_W - \langle z^2 \rangle_{W0})$ and $S_I(\Delta \langle z^2 \rangle)$, agree within a few percent over most of the energy range we studied, except at the point of lowest measured energy, where they differ by 10%. The results show clearly that the shape of the entropy curve of a weakly interacting Fermi gas is nearly identical to that of an ideal gas when the mean field shift of the ground state size is included by referring the mean square cloud size to that of the ground state. So we have to a good approximation,

$$S = S_W(\langle z^2 \rangle_W - \langle z^2 \rangle_{W0}) \simeq S_I(\langle z^2 \rangle_W - \langle z^2 \rangle_{W0}). \quad (8)$$

Since the corrections to ideal gas behavior are small, the determination of S_{1200} by measuring the axial mean square size $\langle z^2 \rangle_{1200}$ relative to the ground state pro-

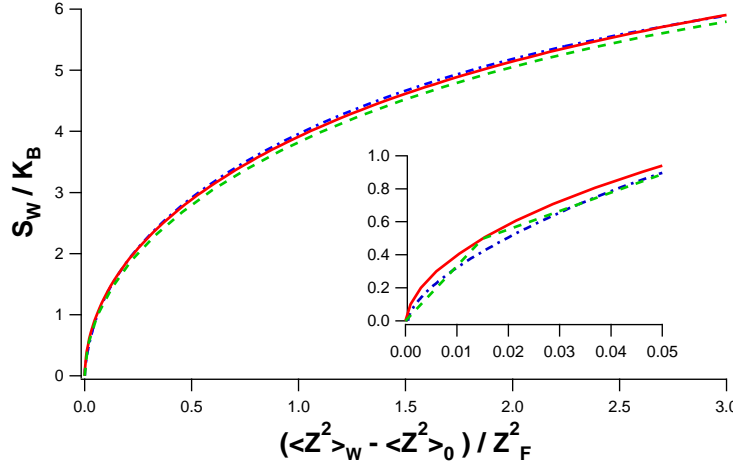


Fig. 1 Color online. Comparison of the entropy versus mean square size curves of a weakly interacting Fermi gas with $k_F a_S = -0.75$ in a gaussian trap with that of a noninteracting Fermi gas. Many-body predictions are shown as the green dashed curve⁴ and the blue dot-dashed curve⁷. The red solid curve is our calculation for a noninteracting gas⁴⁷. All of the calculations employ the gaussian potential of Eq. 3 with a trap depth $U_0/E_F = 10$. The points where $S = 0$ automatically coincide, since the entropy is determined in all cases as a function of mean square size relative to that of the ground state. This corrects approximately for the mean-field shift of the mean square size. Note that for a weakly interacting gas, $\langle z^2 \rangle_0$ is the calculated ground cloud size for each theory that includes the mean field energy shift, while for the noninteracting case $\langle z^2 \rangle_0$ is $\langle z^2 \rangle_{I0}$, the value for an ideal trapped Fermi gas. z_F^2 is the mean square size for an energy $E = E_F$.

vides an essentially model-independent estimate of the entropy of the strongly interacting gas.

2.3 Sound Velocity Measurement

Sound velocity measurements have been implemented for Fermi gases that are nearly in the ground state, from the molecular BEC regime to the weakly interacting Fermi gas regime²². A sound wave is excited in the sample by using a thin slice of green light that bisects the cigar-shaped cloud. The green light at 532 nm is blue detuned from the 671 nm transition in lithium, creating a knife that locally repels the atoms. The laser knife is pulsed on for 280 μ s, much shorter than typical sound propagation times ~ 10 ms and excites a ripple in the density consisting of low density valleys and high density peaks. After excitation, the density ripple propagates outward along the axial direction z . After a variable amount of propagation time, we release the cloud, let it expand, and image destructively. In the strongly interacting regime, we use zero-temperature Thomas-Fermi profiles for a non-interacting Fermi gas to fit the density profiles, and locate the positions of the density valley and peak. By recording the position of the density ripple versus the propagation time, the sound velocity is determined. A detailed discussion of potential sources of systematic error is given by Joseph et al.²².

For a strongly interacting Fermi gas in the unitary limit, the sound velocity c_0 at the trap center for the ground state is determined by the Fermi velocity of an ideal gas at the trap center, $v_F = (2E_F/m)^{1/2}$ and the universal constant β ,

$$\frac{c_0}{v_F} = \frac{(1 + \beta)^{1/4}}{\sqrt{5}}. \quad (9)$$

A precision measurement of the sound speed therefore enables a determination of β ²². As discussed below, the values of β determined from the $E(S)$ data and the sound velocity data are in very good agreement.

3 Comparison of Thermodynamic Data with Theory

In the experiments, the raw data consists of the measured mean square cloud sizes at 840 G and after an adiabatic sweep of the magnetic field to 1200 G. Using this data, we determine both the energy and the entropy of the strongly interacting gas. The data is then compared to several recent predictions.

3.1 Mean Square Cloud Sizes

We begin by determining the axial mean square cloud sizes at 840 G and after the adiabatic sweep to 1200 G. Since the atom number can vary between different runs by up to 20%, it is important to make the comparison independent of the atom number and trap parameters. For this purpose, the mean square sizes are given in units of $z_F^2(B)$, as defined above.

The measured mean square sizes are listed in Table 1. In the experiments, evaporative cooling is used to produce an atom cloud near the ground state. Energy is controllably added by releasing the cloud and then recapturing it after a short time t_{heat} as described previously³⁸. For a series of different values of t_{heat} , the energy at 840 G is directly measured from the axial cloud size according to Eq. 6. Then the same sequence is repeated, but the cloud size is measured after an adiabatic sweep to 1200 G. In each case, the systematic increase in mean square size arising from background heating rate is determined and subtracted. The total data comprise about 900 individual measurements of the cloud size at 840 G and 900 similar measurements of the cloud size after a sweep to 1200 G. To estimate the measurement error, we split the energy scale at 840 G into bins with a width of $\Delta E = 0.04 E_F$. Measured data points within the width of the energy bin are used to calculate the average measured values of the cloud sizes and the corresponding standard deviation at both 840 G and 1200 G.

The ratio of the mean square axial cloud size at 1200 G (measured after the sweep) to that at 840 G (measured prior to the sweep) is plotted in Fig. 2 as a function of the energy of a strongly interacting gas at 840 G. The ratio is ≥ 1 , since for an adiabatic sweep of the magnetic field from the strongly interacting regime to the weakly interacting regime, the total entropy in the system is conserved but the energy increases: The strongly interacting gas is more attractive than the weakly interacting gas. A similar method was used to measure the potential energy change

	$\langle z^2 \rangle_{840}/z_F^2(840)$	$\langle z^2 \rangle_{1200}/z_F^2(1200)$	E_{840}/E_F	S_{1200}/k_B	S_{1200}^*/k_B	S_{1200}^{**}/k_B
1	0.568(4)	0.743(6)	0.548(4)	0.63(8)	0.91(23)	0.97(5)
2	0.612(5)	0.776(13)	0.589(5)	0.99(11)	1.18(22)	1.24(9)
3	0.661(5)	0.803(11)	0.634(5)	1.22(8)	1.36(20)	1.42(7)
4	0.697(9)	0.814(15)	0.667(8)	1.30(10)	1.43(18)	1.49(8)
5	0.74(1)	0.87(4)	0.71(1)	1.6(2)	1.72(18)	1.8(2)
6	0.79(1)	0.89(2)	0.75(1)	1.7(1)	1.79(15)	1.9(1)
7	0.83(1)	0.94(2)	0.79(1)	2.0(1)	2.03(16)	2.1(1)
8	0.89(2)	1.02(2)	0.84(2)	2.3(1)	2.32(18)	2.4(1)
9	0.91(1)	1.02(3)	0.86(1)	2.3(1)	2.31(16)	2.4(1)
10	0.97(1)	1.10(1)	0.91(1)	2.55(4)	2.57(17)	2.64(4)
11	1.01(1)	1.17(2)	0.94(1)	2.74(7)	2.75(19)	2.82(7)
12	1.05(1)	1.18(1)	0.98(1)	2.78(4)	2.80(17)	2.87(4)
13	1.10(1)	1.22(1)	1.03(1)	2.89(2)	2.90(15)	2.97(2)
14	1.25(2)	1.35(5)	1.15(1)	3.21(12)	3.20(14)	3.27(12)
15	1.28(1)	1.39(3)	1.18(1)	3.28(6)	3.28(14)	3.35(6)
16	1.44(2)	1.49(2)	1.31(2)	3.49(4)	3.48(9)	3.55(4)
17	1.53(2)	1.62(6)	1.39(2)	3.74(10)	3.73(11)	3.80(10)
18	1.58(1)	1.63(1)	1.42(1)	3.76(2)	3.74(8)	3.81(2)
19	1.70(2)	1.73(6)	1.52(1)	3.94(9)	3.92(7)	3.99(9)
20	1.83(5)	1.79(2)	1.62(4)	4.03(3)	4.01(1)	4.08(3)
21	1.93(3)	1.96(3)	1.70(2)	4.28(4)	4.26(6)	4.32(4)
22	2.11(5)	2.17(3)	1.83(4)	4.55(3)	4.53(7)	4.59(3)

Table 1 Mean square axial cloud size, energy, and entropy measured in a trapped strongly interacting Fermi gas. $\langle z^2 \rangle_{840}/z_F^2(840)$ is the scaled axial mean square size at 840 G. $\langle z^2 \rangle_{1200}/z_F^2(1200)$ is the scaled axial mean square size at 1200 G. E_{840}/E_F is the energy per particle of a strongly interacting Fermi gas at 840 G, calculated using Eq. 6. S_{1200}/k_B is the corresponding entropy per particle of the gas after an adiabatic sweep of magnetic field from 840 G to 1200 G, where the noninteracting entropy curve (for the gaussian trap) is used to determine the entropy at 1200 G and the ground state mean square size is assumed to be $\langle z^2 \rangle_0 = 0.71 z_F^2(1200)$. S_{1200}^{**}/k_B is the ideal gas entropy result assuming $\langle z^2 \rangle_0 = 0.69 z_F^2(1200)$. S_{1200}^*/k_B is the entropy obtained using an exact many-body calculation for $k_F a = -0.75^4$.

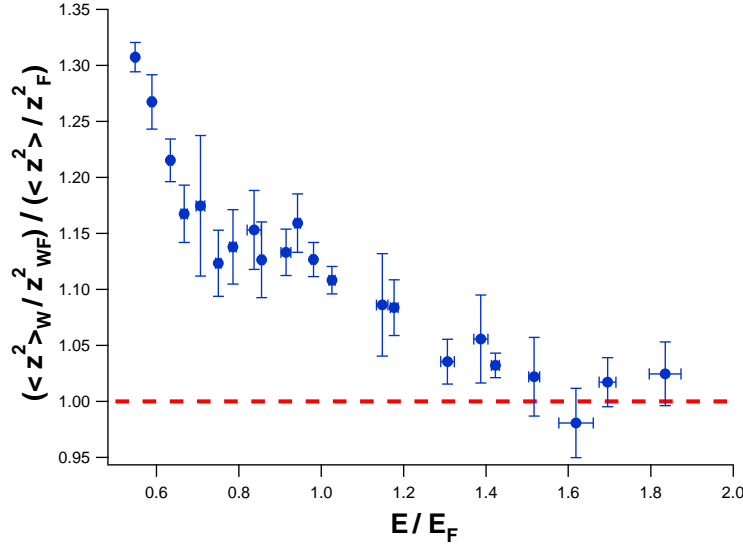


Fig. 2 Color online. The ratio of the mean square cloud size at 1200 G, $\langle z^2 \rangle_{1200}$, to that at 840 G, $\langle z^2 \rangle_{840}$, for an isentropic magnetic field sweep. E is the total energy per particle of the strongly interacting gas at 840 G and E_F is the ideal gas Fermi energy at 840 G. The ratio converges to unity at high energy as expected (the dashed line). Here, z_{WF} is evaluated at 1200 G, while z_F is evaluated at 840 G (see text).

in a Fermi gas of ^{40}K , where the bias magnetic field was adiabatically swept between the strongly interacting regime at the Feshbach resonance and a noninteracting regime above resonance⁴⁸. The resulting potential energy ratios are given as a function of the temperature of the noninteracting gas⁴⁸. In contrast, by exploiting the virial theorem which holds for the unitary gas, we determine both the energy and entropy of the strongly interacting gas, as described below.

3.2 Energy versus Entropy

Fig. 3 shows the entropy which is obtained from the mean square size at 1200 G $\langle z^2 \rangle_{1200} / z_F^2(1200)$ as listed in Table 1. First, we find the mean square size relative to that of the ground state, $(\langle z^2 \rangle_{1200} - \langle z^2 \rangle_0) / z_F^2(1200)$. We use the measured value $\langle z^2 \rangle_0 = 0.71 z_F^2(1200)$ for the lowest energy state that we obtained at 1200 G, as determined by extrapolation to $T = 0$ using a Sommerfeld expansion for the spatial profile of an ideal Fermi gas. Then we determine the entropy in the noninteracting ideal Fermi gas approximation: $S_I[\langle z^2 \rangle_{1200} - \langle z^2 \rangle_0]$, where we have replaced $\langle z^2 \rangle_{I0}$ by the ground state value at 1200 G. As discussed above, this method automatically ensures that $S = 0$ corresponds to the measured ground state $\langle z^2 \rangle_0$ at 1200 G, and compensates for the mean field shift between the measured $\langle z^2 \rangle_0$ for a weakly interacting Fermi gas and that calculated $\langle z^2 \rangle_{I0} = 0.77 z_F^2$ for an ideal Fermi gas in our gaussian trapping potential. As shown in Fig. 1, the entropy obtained from a more precise many-body calculations is in close agreement with the ideal gas

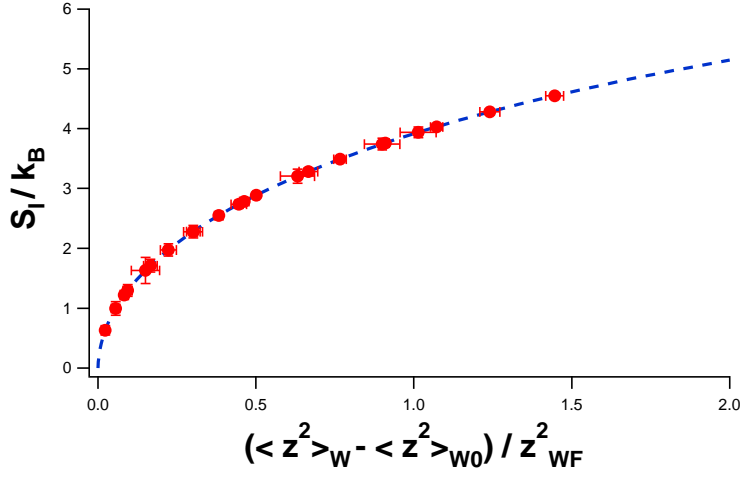


Fig. 3 Color online. The conversion of the mean square size at 1200 G to the entropy. The dashed line is the calculated entropy for a noninteracting Fermi gas in the Gaussian trap with $U_0/E_F = 10$. $\langle z^2 \rangle_0 = 0.71 z_F^2$ is the measured ground state size for a weakly interacting Fermi gas. The calculated error bars of the entropy are determined from the measured error bars of the cloud size at 1200 G. Here, z_{WF} is evaluated at 1200 G.

entropy calculated in the ideal gas approximation. The energy is determined from the cloud profiles at 840 G using Eq. 6.

Finally, we generate the energy-entropy curve for a strongly interacting Fermi gas, as shown in Fig. 4. Here, the energy E measured from the mean square axial cloud size at 840 G is plotted as a function of the entropy S measured at 1200 G after an adiabatic sweep of the magnetic field. We note that above $S = 4k_B$ ($E = 1.5E_F$) the $E(S)$ data (blue dots) for the strongly interacting gas appear to merge smoothly to the ideal gas curve (dashed green).

In addition to the entropy calculated in the ideal gas approximation, Table 1 also provides a more precise entropy $S^*(1200)$ versus the axial mean square cloud size. These results are obtained by Hu et al.⁴ using a many-body calculation for $k_F a = -0.75$ at 1200 G in the gaussian trap of Eq. 3.

3.3 Testing Predictions from Many-Body Theories

Perhaps the most important application of the energy-entropy measurements is to test strong coupling many-body theories and simulations. Since the energy and entropy are obtained in absolute units without invoking any specific theoretical model, the data can be used to distinguish recent predictions for a trapped strongly interacting Fermi gas.

Fig. 5 shows how four different predictions compare to the measured energy and entropy data. These include a pseudogap theory^{8,49}, a combined Luttinger-Ward-De Dominicis-Martin (LW-DDM) variational formalism⁶, a T-matrix calculation using a modified Nozières and Schmitt-Rink (NSR) approximation^{4,5}, and a quantum Monte Carlo simulation^{7,50}. The most significant deviations ap-

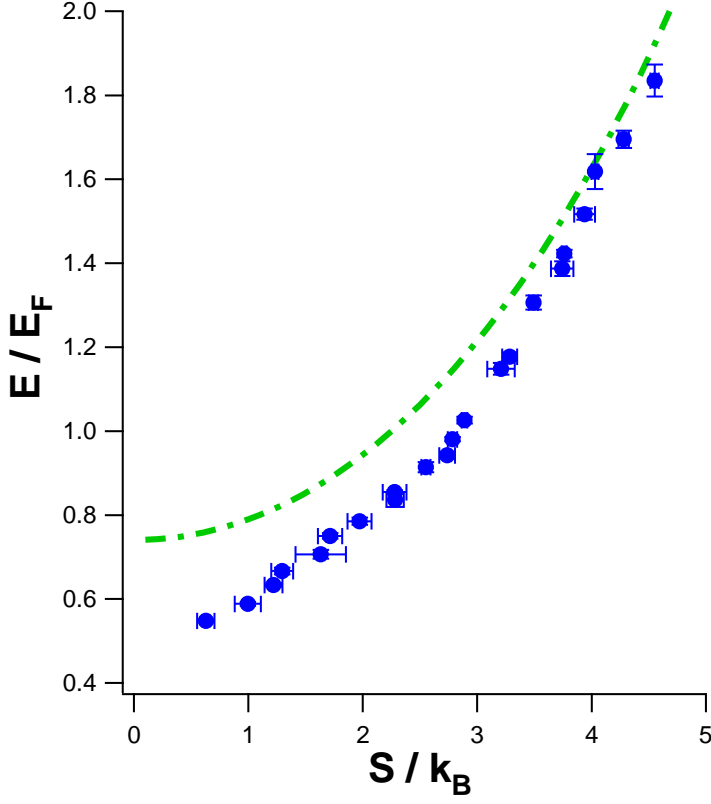


Fig. 4 Color online. Measured total energy per particle of a strongly interacting Fermi gas at 840 G versus its entropy per particle. For comparison, the dot-dashed green curve shows $E(S)$ for an ideal Fermi gas. For this figure, the ideal gas approximation to the entropy is used, S_{1200}/k_B of Table 1.

pear to occur near the ground state, where the precise determination of the energy seems most difficult. The pseudogap theory predicts a ground state energy that is above the measured value while the prediction of Ref.⁶ is somewhat low compared to the measurement. All of the different theories appear to converge at the higher energies.

4 Determining the Temperature and Critical Parameters

The temperature T is determined from the measured $E(S)$ data using the fundamental relation, $T = \partial E / \partial S$. To implement this method, we need to parameterize the data to obtain a smooth differentiable curve.

At low temperatures, one expects the energy to increase from the ground state according to a power law in T and a corresponding power law in S , i.e., $E = E_0 + aS^b$. For a harmonically trapped ideal Fermi gas, we have in the Sommerfeld approximation an energy per particle in units of E_F given by $E = 3/4 +$

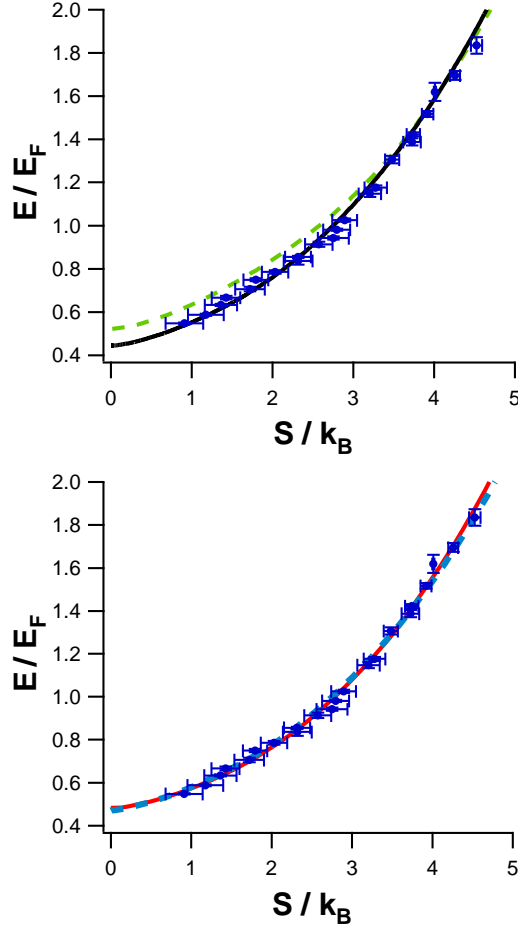


Fig. 5 Color online. Comparison of the experimental energy versus entropy data with the calculations from strong coupling many-body theories. Top: The green dashed curve is a pseudogap theory^{8,49}. The black solid curve is a LW-DDM variational calculation⁶. For this figure, the entropy is given by S_{1200}^*/k_B in Table 1. Bottom: The blue dashed curve is an NSR calculation^{4,5}. The red solid curve is a quantum Monte Carlo simulation^{7,50}. For this figure, the entropy is given by S_{1200}^*/k_B in Table 1.

$\pi^2(T/T_F)^2/2$. The corresponding entropy per particle in units of k_B is $S = \pi^2(T/T_F)$, so that $E = 3/4 + S^2/(2\pi^2) \simeq 0.75 + 0.05 S^2$.

4.1 Power Law Fit and Temperature for an Ideal Fermi Gas

We attempt to use a single power law to fit the $E_I(S)$ curve for a noninteracting Fermi gas in a gaussian trapping potential, with $U_0/E_F = 10$, as in our experiments. The energy and entropy are calculated in the energy range $0.75E_F \leq$

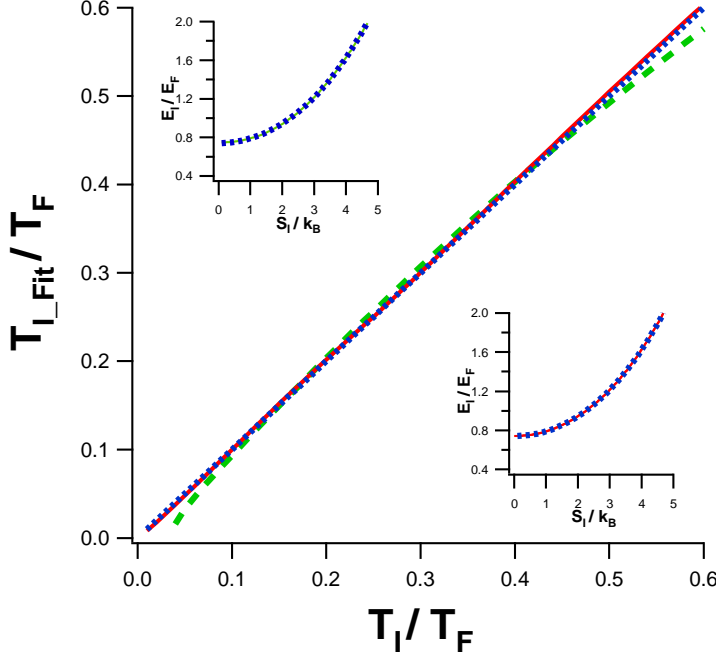


Fig. 6 Color online. The inset top left shows a single power-law fit to the calculated energy versus entropy per particle of a noninteracting Fermi gas in a gaussian trap. The exact result (blue dots) is well fit by the single power law function (green solid curve) $E_I = (0.747 \pm 0.001) + (0.0419 \pm 0.0004) S^{(2.197 \pm 0.006)}$. The inset bottom right shows a two-power law fit to the calculated energy versus entropy per particle of a noninteracting Fermi gas in a gaussian trap. The exact $E_I(S)$ (blue dots), is very well fit by the two power law function (red solid curve) of Eq. 12 for $e \neq 0$ with $a = 0.0480(2)$, $b = 2.08(3)$, $S_c = 2.16(3)$, $d = 2.483(7)$ and $E_0 = 0.7415(2)$. The temperature of a noninteracting Fermi gas obtained from the fits to the calculated energy versus entropy is compared to the exact temperature. The blue dotted line corresponds to exact agreement. The green dot-dashed curve is from the single power law fit showing deviation only at the highest and lowest temperatures. The red curve is from two power law fit of Eq. 12 with $e \neq 0$ showing excellent agreement over the full range.

$E \leq 2E_F$ and displayed as dots in Fig. 6. We find that a single power law $E_I = (0.747 \pm 0.001) + (0.0419 \pm 0.0004) S^{(2.197 \pm 0.006)}$ fits the curve very well over this energy range. Note that the power law exponent is $b \simeq 2$, close to the low temperature value.

Using the fit function, we can extract the reduced temperature $T_{I,fit}/T_F = \partial E_I / \partial S_I$ as a function of S_I and compare it to the theoretical reduced temperature T/T_F at the same S_I . The results are shown as the green dashed line in Fig. 6. We see that the agreement is quite good except below $T/T_F = 0.1$ and above 0.5 , where the deviation is $\simeq 10\%$.

To improve the fit and to make a more precise determination of the temperature, we employ a fit function comprising two power laws that are joined at a certain entropy S_c , which gives the best fit. When used to fit the data for the strongly interacting Fermi gas, we consider two types of fits that incorporate either a jump

in heat capacity or a continuous heat capacity at S_c . In this way, we are able to determine the sensitivity of the temperature and critical parameters to the form of the fit function. The two types of fits yield nearly identical temperatures, but different values of S_c and hence of the critical parameters, as discussed below.

We take the energy per particle E in units of E_F to be given in terms of the entropy per particle in units of k_B in the form

$$\begin{aligned} E_{<}(S) &= E_0 + aS^b; \quad 0 \leq S \leq S_c \\ E_{>}(S) &= E_1 + cS^d + e(S - S_c)^2; \quad S \geq S_c. \end{aligned} \quad (10)$$

We constrain the values of E_1 and c by demanding that energy and temperature be continuous at the joining point S_c :

$$\begin{aligned} E_{<}(S_c) &= E_{>}(S_c) \\ \left(\frac{\partial E_{<}}{\partial S} \right)_{S_c} &= \left(\frac{\partial E_{>}}{\partial S} \right)_{S_c}. \end{aligned} \quad (11)$$

By construction, the value of e does not affect these constraints and is chosen in one of two ways. Fixing $e = 0$, the fit incorporates a heat capacity jump at S_c , which arises from the change in the power law exponents at S_c . Alternatively, we choose e so that the second derivative $E''(S)$ is continuous at S_c , making the heat capacity continuous. The final fit function has 5 independent parameters E_0, S_c, a, b, d , and takes the form

$$\begin{aligned} E_{<}(S) &= E_0 + aS^b; \quad 0 \leq S \leq S_c \\ E_{>}(S) &= E_0 + aS_c^b \left[1 - \frac{b}{d} + \frac{b}{d} \left(\frac{S}{S_c} \right)^d \right] + e(S - S_c)^2; \quad S \geq S_c. \end{aligned} \quad (12)$$

Here, when e is not constrained to be zero, it is given by

$$e = \frac{ab}{2}(b-d)S_c^{b-2} \quad (13)$$

Fig. 6 shows the improved fit to the calculated energy versus entropy of a noninteracting Fermi gas in a gaussian trap for $U_0/E_F = 10$, using Eq. 12 with $e \neq 0$, since the ideal gas has no heat capacity jump. In this case, both power law exponents b and d are close to 2 as for the single power law fit. The temperature determined from the fit agrees very closely with the exact temperature, as shown in Fig. 6 (red solid line).

4.2 Power Law Fit and Temperature of a Strongly Interacting Fermi Gas

In contrast to the noninteracting case, we have found that the energy-entropy data of a strongly interacting Fermi gas is not well fit by a single power law function³⁸. However, the two power-law function fits quite well, with a factor of two smaller value of χ^2 than for the single power-law fit. Here, we use $\chi^2 = \sum_i (\frac{y - y_i}{\sigma_i})^2$, where y (y_i) is the fitted (data) value for the i^{th} point, and σ_i is the corresponding the standard error.

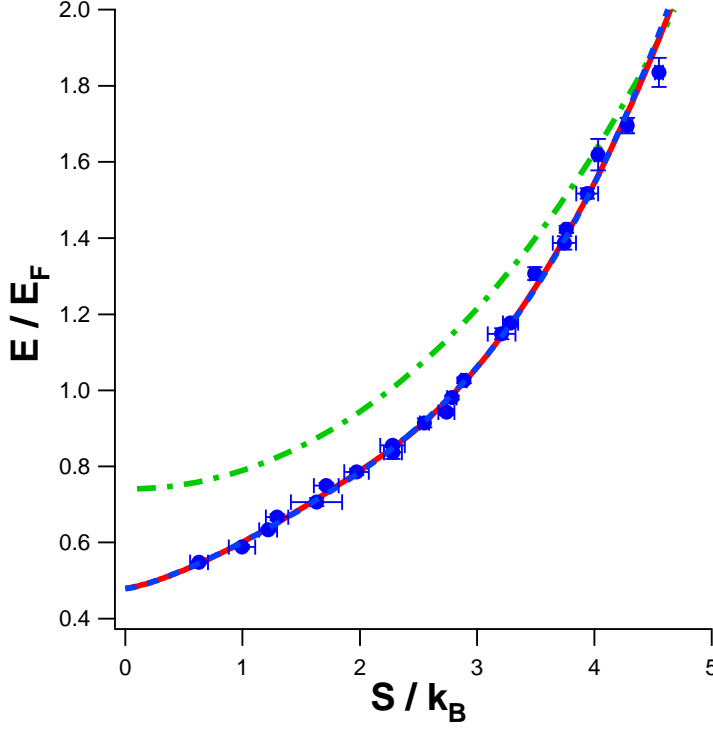


Fig. 7 Color online. To determine the temperature, the energy-entropy data are parameterized by joining two power-law fit functions. The red solid line shows the fit that includes a heat capacity jump, while the blue dashed curve shows the fit for a continuous heat capacity (see § 4). For comparison, the dot-dashed green curve shows $E(S)$ for an ideal Fermi gas. For this figure, the ideal gas approximation to the entropy is used, S_{1200}/k_B of Table 1.

Motivated by the good fits of the two power-law function to the ideal gas energy versus entropy curve and the good agreement between the fitted curve and exact temperature, we apply the two power-law fit function to the data for the strongly interacting Fermi gas.

Fig. 7 shows the fit (red solid curve) obtained with a heat capacity jump using Eq. 12 with $e = 0$ and $a = 0.12(1)$, $b = 1.35(11)$, $d = 2.76(12)$, the ground state energy $E_0 = 0.48(1)$, and the critical entropy $S_c = 2.2(1)$. Also shown is the fit (blue dashed curve) with continuous heat capacity ($e \neq 0$) and $a = 0.12(2)$, $b = 1.31(17)$, $d = 2.9(2)$, the ground state energy $E_0 = 0.48(2)$, and the critical entropy $S_c = 1.57(29)$.

4.3 Estimating the Critical Parameters

The fit functions for the $E(S)$ data for the strongly interacting Fermi gas exhibit a significant change in the scaling of E with S below and above S_c . The dramatic change in the power law exponents for the strongly interacting gas suggests a transition in the thermodynamic properties. The power law exponent is 2.9 above

	$S_c(k_B)$	$E_c(E_F)$	$T_c(T_F)$
Expt $E(S)$ Fit ¹	2.2(1)	0.83(2)	0.21(1)
Expt $E(S)$ Fit ²	1.6(3)	0.70(5)	0.185(15)
Heat Capacity Experiment*		0.85	0.20
Theory Ref. ⁹			0.30
Theory Ref. ¹¹			0.31
Theory Ref. ⁸			0.27
Theory Ref. ⁴			0.29
Theory Ref. ⁷	2.15	0.82	0.27
Theory Ref. ⁶	1.61(5)	0.667(10)	0.214(7)

Table 2 Critical parameters for a strongly interacting Fermi gas. The experimental results are obtained from fits to the energy versus entropy data using Eq. 12: Fit¹ uses $e = 0$, and has a jump in heat capacity. Fit² constrains e so that there is no jump in heat capacity. The theoretical results are presented for comparison. *Using the present experimental calibration of the measured empirical transition temperature, see § 5.3.

S_c , comparable to that obtained for the ideal gas, where $d = 2.5$. The power law exponent below S_c is 1.35, which corresponds to the low temperature dependence $E - E_0 \propto T^{3.86}$, close to that obtained in measurements of the heat capacity, where the observed power law was 3.73 after the model-dependent calibration of the empirical temperature³⁷, see § 5.3.

If we interpret S_c as the critical entropy for a superfluid-normal fluid transition in the strongly interacting Fermi gas, then we can estimate the critical energy E_c and the critical temperature $T_c = (\partial E_<(S)/\partial S)_{S_c}$. For the fits of Eq. 12 with a heat capacity jump ($e = 0$) or with continuous heat capacity ($e \neq 0$), we obtain

$$\begin{aligned} E_c &= E_0 + a S_c^b \\ T_c &= ab S_c^{b-1}. \end{aligned} \quad (14)$$

Using the fit parameters in Eq. 14 yields critical parameters of the strongly interacting Fermi gas, which are summarized in Table 2. The statistical error estimates are from the fit, and do not include systematic errors arising from the form of the fit function.

We note that the fit function for $S(E)$ previously used in Ref.³⁸ to determine the temperature was continuous in S and E , but intentionally ignored the continuous temperature constraint in order to determine the entropy as a power of $E - E_0$ both above and below the joining energy E_c . As the continuous temperature constraint is a physical requirement, we consider the present estimate of the temperature T to be more useful for temperature calibrations and for characterizing the physical properties of the gas than the estimate of Ref.³⁸.

In contrast to the temperature T , the estimate of T_c depends on the value of the joining entropy S_c that optimizes the fit and is more sensitive to the form of fit function than the temperature that is determined from the E and S data. For the fit

function $S(E)$ used in Ref. ³⁸, the temperatures determined by the fit function just above E_c , $T_{c>}$, and below E_c , $T_{c<}$, were different. An average of the slopes $1/T_{c>}$ and $1/T_{c<}$ was used to estimate the critical temperature. From those fits, the critical energy was found to be $E_c/E_F = 0.94 \pm 0.05$, the critical entropy per particle was $S_c = 2.7(\pm 0.2)k_B$. The estimated critical temperature obtained from the average was $T_c/T_F = 0.29(+0.03/-0.02)$, significantly higher than the value $T_c/T_F = 0.21$ obtained using Eq. 12, which incorporates continuous temperature.

We are able to substantiate the critical temperature $T_c/T_F = 0.21$ by using our data to experimentally calibrate the temperature scales in two other experiments. In § 5.2, we find that this value is in very good agreement with the estimate we obtain by calibrating the ideal gas temperature observed for the onset of pair condensation. Nearly the same transition temperature is obtained in § 5.3 by using the $E(S)$ data to calibrate the empirical transition temperature measured in heat capacity experiments³⁷.

Table 2 compares the critical parameters estimated from the power-law fits to the $E(S)$ data with the predictions for a trapped unitary Fermi gas from several theoretical groups. We note that calculations for a uniform strongly interacting Fermi gas at unitarity⁵¹ yield a lower critical temperature, $T_c/T_F(n) = 0.152(7)$, than that of the trapped gas, where $T_F(n)$ is the Fermi temperature corresponding to the uniform density n . Extrapolation of the uniform gas critical temperature to that of the trapped gas shows that the results are consistent⁶.

Using the parameters from the fits and Eq. 12, the temperature of the strongly interacting Fermi gas, in units of T_F can be determined as a function of the entropy per particle, in units of k_B ,

$$\begin{aligned} T_{<}(S) &= T_c \left(\frac{S}{S_c} \right)^{b-1}; \quad 0 \leq S \leq S_c \\ T_{>}(S) &= T_c \left(\frac{S}{S_c} \right)^{d-1} + 2e(S - S_c); \quad S \geq S_c. \end{aligned} \quad (15)$$

Here S_c is given in Table 2 from the fits to the $E(S)$ data for the strongly interacting gas, Eq. 14 gives T_c . Fig. 8 shows the temperature as a function of entropy according to Eq. 15 for fits with a heat capacity jump and for continuous heat capacity.

5 Temperature Calibrations

The estimates of the temperature of the strongly interacting Fermi gas as a function of the entropy can be used to experimentally calibrate the temperatures measured in other experiments, without invoking any specific theoretical models. The JILA group measures the pair condensate fraction in a strongly interacting Fermi gas of ⁴⁰K as a function of the initial temperature T_{Ic} in the noninteracting regime above the Feshbach resonance^{26,31}. In these experiments, a downward adiabatic sweep of the bias magnetic field to resonance produces a strongly interacting sample. Using our $E(S)$ data, we relate the endpoint temperatures for adiabatic sweeps of the bias magnetic field between the ideal and strongly interacting Fermi gas regimes. We therefore obtain the critical temperature for the onset of pair condensation in the

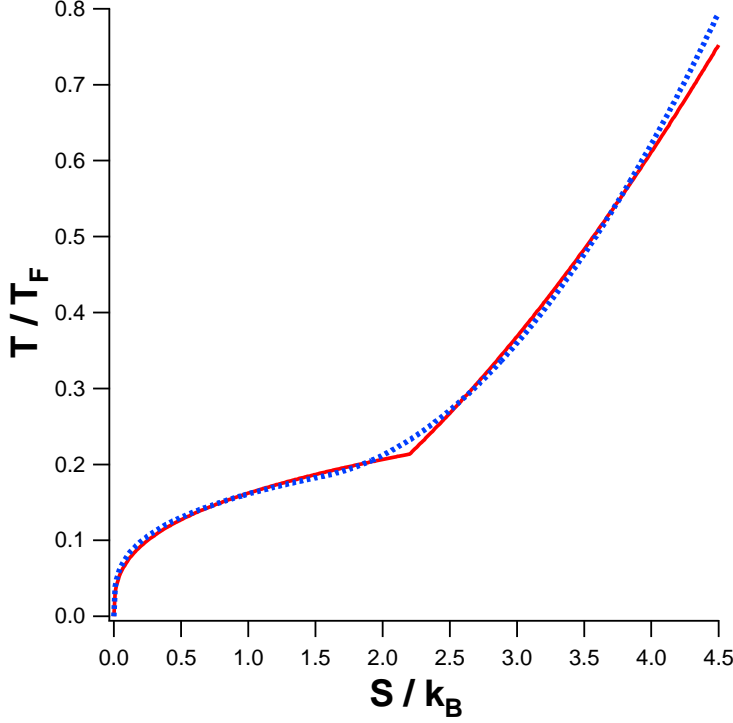


Fig. 8 Color online. The temperature versus the entropy of a strongly interacting Fermi gas from the fits to the $E(S)$ measurement. The red solid curve is given by Eq. 15 for $e = 0$ (heat capacity jump) and the blue dotted curve is for $e \neq 0$ (continuous heat capacity).

strongly interacting Fermi gas, and find very good agreement with our estimates based on entropy-energy measurement.

In addition, we calibrate the empirical temperature based on the cloud profiles, which was employed in our previous measurements of the heat capacity³⁷.

5.1 Endpoint Temperature Calibration for Adiabatic Sweeps

We relate the endpoint temperatures for an adiabatic sweep between the strongly interacting and ideal Fermi gas regimes. Eq. 15 gives the temperature of the strongly interacting gas as a function of entropy, i.e., $T(S)$.

Next, we calculate the entropy per particle $S_I(T_I)$ for an ideal Fermi gas in our gaussian trap, in units of k_B , with T_I in units of T_F , as used in § 4.1 to determine $E_I(S_I)$. For an adiabatic sweep between the strongly interacting and ideal Fermi gas regimes, where $S = S_I$, the temperature of the strongly interacting gas is related to that for the ideal Fermi gas by

$$T = T[S_I(T_I)], \quad (16)$$

which is shown in Fig. 9.

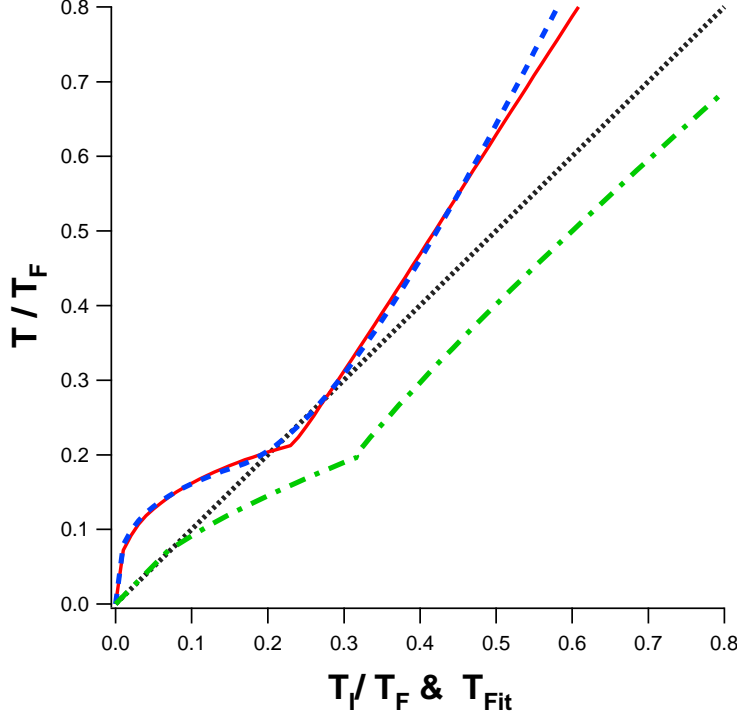


Fig. 9 Color online. Experimental temperature calibrations: Temperature of a strongly interacting Fermi gas (T/T_F) compared to the temperature of a noninteracting Fermi gas (T_I/T_F) for an adiabatic sweep between and strongly interacting and ideal Fermi gas regimes (equal entropies). The solid red curve is obtained from the fit to the $E(S)$ data with a heat capacity jump and the dashed blue curve is obtained from the fit with continuous heat capacity. The dashed green curve shows the value of the empirical temperature T_{fit} , as obtained from the cloud profiles in Ref.³⁷, versus the corresponding reduced temperature of the strongly interacting Fermi gas at the same energy. The dotted black line denotes equal temperatures.

For an adiabatic sweep from the ideal Fermi gas regime to the strongly interacting Fermi gas regime at low temperature $T < T_c$, the reduced temperature of the strongly interacting gas is greater than or equal to that of the ideal gas. This arises because the entropy of the strongly interacting gas scales as a higher power of the temperature than that of the ideal gas.

In our present experiments, we could not take data at high enough temperatures to properly characterize the approach of the temperature to the ideal gas regime. Above T_c , our $E(S)$ data are obtained over a limited range of energies $E \leq 2E_F$ to avoid evaporation in our shallow trap. In this energy range, our data are reasonably well fit by a single power law. However, such a power law fit cannot completely describe the higher temperature regime. We expect that the temperatures of the strongly interacting gas and ideal gas must start to merge in the region $S \cong 4k_B$, where the $E(S)$ data for the strongly interacting gas nearly overlaps with the $E(S)$ curve for an ideal gas, as shown in Fig. 4.

From Fig. 8, $S > 4k_B$ corresponds to $T/T_F > 0.6$, approximately the place where the calibrations from the two different power law fits (for $e = 0$ and $e \neq 0$) begin to differ in Fig. 9. We therefore expect that the single power law fit overestimates the temperature T of the strongly interacting gas for $T > 0.6T_F$, yielding a trend away from ideal gas temperature, in contrast to the expected merging at high temperature.

5.2 Critical Temperature for the Onset of Pair Condensation

In Ref.²⁶, projection experiments measure the ideal Fermi gas temperature T_{Ic} where pair condensation first appears. In those experiments, T_{Ic} is estimated to be $0.18(2)T_F$ ³¹. From the calibration, Fig. 9, we see that for $T_{Ic} = 0.18T_F$, the corresponding temperature of the strongly interacting gas is $T_c = 0.19(2)T_F$ for both the red solid and blue dashed curves, which is almost the same as the ideal gas value. The critical temperature of the strongly interacting gas for the onset of pair condensation is then $0.19(2)T_F$, in very good agreement with the values $T_c = 0.21(1)T_F$ and $T_c = 0.185(15)T_F$ that we obtain from the two fits to the $E(S)$ measurements. This substantiates the conjecture that the change in the power law behavior observed at T_c in our experiments corresponds to the superfluid transition.

5.3 Calibrating the Empirical Temperature obtained from the Cloud Profiles

In our previous study of the heat capacity, we determined an empirical temperature $T_{fit} \equiv \tilde{T}$ as a function of the total energy of the gas^{37,19}. The gas was initially cooled close to the ground state and a known energy was added by a release and recapture method. Then a Thomas-Fermi profile for an ideal Fermi gas was fit to the low temperature cloud profiles to determine the Fermi radius. Holding the Fermi radius constant, the best fit to the cloud profiles at higher temperatures determined the effective reduced temperature, which is denoted \tilde{T} . The $E(\tilde{T})$ data³⁷ was observed to scale as $E - E_0 = 1.54E_F \tilde{T}^{1.43}$ for $\tilde{T} \geq 0.33$, while below $\tilde{T} = 0.33$, the energy was found to scale as $E - E_0 = 4.9E_F \tilde{T}^{2.53}$. The transition point occurs at an energy $E_c = 0.85E_F$, which is close to the value $0.83E_F$ obtained from power-law fit to the $E(S)$ data for the fit with a heat capacity jump. Assuming that $\tilde{T}_c = 0.33$ corresponds to the superfluid-normal fluid transition, we can determine the corresponding value of T_c/T_F for the strongly interacting gas.

To calibrate the empirical temperature we start with $E(\tilde{T})$. Then, as discussed in § 7.1, Eq. 12 determines $E(T)$ and hence $T(E)$ from the fits to our $E(S)$ data. Hence $T(\tilde{T}) = T[E(\tilde{T})]$, where $T \equiv T/T_F$ is the reduced temperature of the strongly interacting gas and $E \equiv E/E_F$ is the reduced energy. For simplicity, we give the analytic results obtained using the $e = 0$ fit to the $E(S)$ data,

$$\begin{aligned} \frac{T}{T_F} &= 0.42 \tilde{T}^{0.66}; \quad 0 \leq \tilde{T} \leq 0.33 \\ \frac{T}{T_F} &= (0.80 \tilde{T}^{1.43} - 0.09)^{0.64}; \quad \tilde{T} \geq 0.33. \end{aligned} \quad (17)$$

Fig. 9 shows the full calibration (green dashed curve). For comparison, the calibration obtained from the pseudogap theory of the cloud profiles gave $T/T_F = 0.54\tilde{T}^{0.67}$ for $\tilde{T} \leq 0.33$, and $T/T_F = 0.71\tilde{T}$ above $\tilde{T} = 0.33$. For $\tilde{T}_c = 0.33$, we obtain from Eq. 17 $T_c/T_F = 0.20$ (see Fig. 9), in good agreement with the value obtained for the onset of pair condensation and with the values $T_c = 0.185(15)$ and $T_c = 0.21(1)$ determined from the fits to the $E(S)$ data.

6 Measuring the Ground State Energy

Measurement of the ground state energy of a unitary Fermi gas provides a stringent test of competing many-body theoretical predictions and is therefore of great interest. For a unitary Fermi gas of uniform density in a 50-50 mixture of two spin states, the ground state energy per particle can be written as

$$E_g = (1 + \beta) \frac{3}{5} \varepsilon_F(n), \quad (18)$$

where $\varepsilon_F(n)$ is the local Fermi energy corresponding to the density n . The ground state energy of the unitary Fermi gas differs by a universal factor $\xi \equiv 1 + \beta$ from that of an ideal Fermi gas at the same density. The precise value of ξ has been of particular interest in the context of neutron matter^{52,53,54,55}, and can be measured in unitary Fermi gas experiments^{1,56}.

The sound speed at temperatures near the ground state determines β according to Eq. 9. We have made precision measurements of the sound speed in a trapped Fermi gas at the Feshbach resonance²². At 834 G, we vary the density by a factor of 30 to demonstrate universal scaling and obtain the value $c_0/v_F = 0.362(6)$. Using Eq. 9 then yields $\beta = -0.565(15)$. Note that the reference Fermi velocity v_F depends on the Fermi energy of an ideal gas at the trap center and hence on both the trap frequencies and atom number (as $N^{1/6}$), which are carefully measured to minimize systematic errors²². While the energy of the gas as measured from the mean square cloud size was close to the ground state value, the precise temperature of the gas was not determined.

The universal parameter β also can be determined by measuring the ground state energy E_0 of a harmonically trapped unitary Fermi gas, which is given by

$$E_0 = \frac{3}{4} \sqrt{1 + \beta} E_F. \quad (19)$$

Our $E(S)$ data enables a new determination of E_0 by extrapolating the measured energy $E(S)$ to $S = 0$. As pointed out by Hui et al.⁴, this method avoids a systematic error arising when the finite temperature is not determined in the measurements.

From both of our fit functions below S_c , we obtain $E_0/E_F = 0.48(1)$. Eq. 19 yields $\beta = -0.59(2)$. This result is slightly more negative than that obtained in the sound speed experiments, which is reasonable since the sound speed measurements are done at finite temperature. Both results are in very good agreement.

One possible systematic error in these measurements arises from the determination of the atom number. The measurements of β from the sound speed and from the energy-entropy measurements were done in different laboratories. The close

agreement is gratifying, considering that the imaging systems that determine the atom number employed σ_- -polarized light for the sound speed experiments, while the entropy-energy measurements used x -polarized light, for which the resonant optical cross section is a factor of two smaller than for σ_- polarization. To examine the systematic error arising from the atom number determination, we employ a third method to measure β based on the measured ratio of the cloud size at 840 G and at 1200 G, which is number independent.

The ratio of the ground state mean square sizes for the weakly and strongly interacting gases is predicted to be

$$r_0 = \frac{\langle z^2 \rangle_{0,1200}/z_F^2(1200)}{\langle z^2 \rangle_{0,840}/z_F^2(840)} = \frac{0.69}{(3/4)\sqrt{1+\beta}}. \quad (20)$$

Note that we obtain $\langle z^2 \rangle_{0,1200}/z_F^2(1200) = 0.69$ from a mean field calculation⁴⁷, in agreement with that obtained using a many-body calculation^{4,7}.

Our measurements for the ground state mean square size at 1200 G are accomplished by fitting a Sommerfeld expansion of the axial density for an ideal Fermi gas to the cloud profile^{38,56}. The fit determines the Fermi radius σ_z and reduced temperature T/T_F , yielding $\langle z^2 \rangle_{0,1200} = \sigma_z^2/8 = 0.71 z_F^2(1200)$ for $T = 0$, close to the predicted value of 0.69. The ground state energy $E_0 = 0.48 E_F(840)$ at 840 G from the entropy-energy experiments determines the ground state mean square size as $\langle z^2 \rangle_{0,840} = 0.48 z_F^2(840)$. Hence, $r_0 = 0.71/0.48 = 1.48$. The corresponding $\beta = -0.61(2)$ from Eq. 20. Since the mean square sizes are determined from the images and the ratio $z_F^2(840)/z_F^2(1200)$ is number independent, this result shows that the systematic error arising from the number measurement is within the quoted error estimate.

We also can determine β by directly extrapolating to zero entropy the ratio of the axial mean square size of the weakly interacting Fermi gas at 1200 G to that of strongly interacting gas at 840 G. When this is done, we obtain $\beta = -0.58$, in very good agreement with the estimates based on the sound speed and ground state energy.

Finally, we can estimate the correction to the ground state energy arising from the finite scattering length at 840 G, $a_S = -73616a_0$. For the trap conditions in the $E(S)$ measurements, $k_F a_S = -18$, where k_F is the wavevector for an ideal Fermi gas at the trap center. To estimate the true unitary ground state energy at $a_S = \infty$, we first determine the leading order $1/(a_S k_F(n))$ correction to the trapped atom density, where $k_F(n)$ is the local Fermi wavevector corresponding to the density n . The local chemical potential is estimated from Ref.⁵⁷. Using the notation of Eq. 3 and a harmonic approximation, the corrected density yields $\langle r^2/\sigma^2 \rangle = (3/8)[1 - (128/105\pi)(0.64/k_F a_S)]$, where σ is the Fermi radius for the unitary gas. According to the virial theorem (see Eq. 5), the mean square size and energy of the unitary gas are corrected by the same factor. The unitary ground state energy is then

$$E_0(\infty) = \frac{E_0(k_F a_S)}{1 - (128/105\pi)(0.64/k_F a_S)}. \quad (21)$$

For $k_F a_S = -18$, we obtain $E_0(\infty) = 0.986 E_0(-18)$ and the value of $\beta = -0.59(2)$ obtained directly from $E(S=0) = E_0 = 0.48(1)$ is shifted to $\beta = -0.60(2)$. We

	β
$E(S)$ Experiment	-0.59(2)
Sound Velocity Experiment	-0.565(15)
Cloud Size Ratio Experiment	-0.61(2)
Ref. ^{55,58,59}	-0.58(1)
Ref. ⁵⁰	-0.56(3)
Ref. ⁴	-0.599
Ref. ⁶⁰	-0.60(1)
Ref. ⁶	-0.646(4)

Table 3 Universal interaction parameter β .

also obtain the corrected value of $r_0 = 0.71/(0.986 * 0.48) = 1.50$ in Eq. 20 and $\beta = -0.62(2)$.

Table 3 compares the values of β obtained in our experiments to several recent predictions. Note that the table does not include the finite $k_F a$ correction for the $E(S)$ measurement at 840 G described above.

7 Universal Thermodynamic Functions

Using the $E(S)$ data for the strongly interacting Fermi gas and the temperature determined from the two power-law fits, we estimate several universal functions. First, we determine the dependence of the energy on temperature $E(T)$ and the corresponding heat capacity, $C(T)$. Then we find the global chemical potential of the trapped gas as a function of the energy $\mu_g(E)$.

7.1 Energy versus Temperature

The energy is readily determined as a function of temperature using Eq. 12 for the case where there is a heat capacity jump and $e = 0$,

$$\begin{aligned}
 E_{<}(T) &= E_c + \frac{S_c T_c}{b} \left[\left(\frac{T}{T_c} \right)^{\frac{b}{b-1}} - 1 \right]; \quad 0 \leq T \leq T_c \\
 E_{>}(T) &= E_c + \frac{S_c T_c}{d} \left[\left(\frac{T}{T_c} \right)^{\frac{d}{d-1}} - 1 \right]; \quad T \geq T_c,
 \end{aligned} \tag{22}$$

where the energy (temperature) is given in units of E_F (T_F) and the critical energy E_c is

$$E_c = E_0 + S_c T_c / b, \tag{23}$$

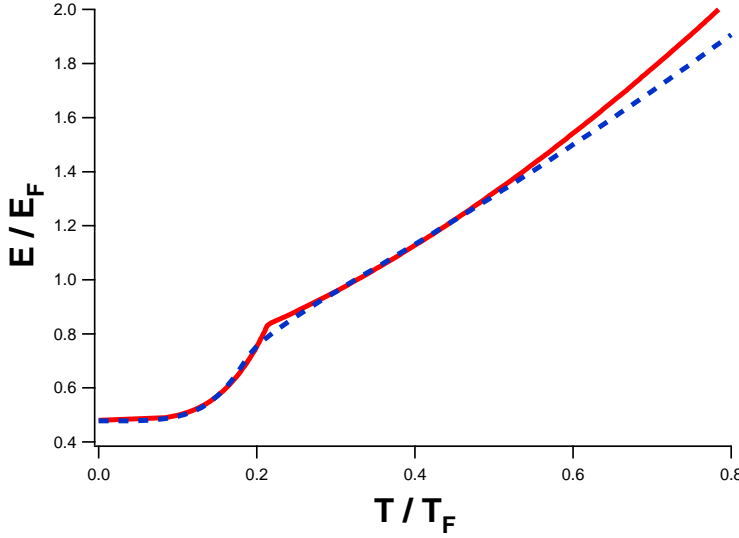


Fig. 10 Color online. The energy of a strongly interacting Fermi gas versus temperature, from the fits to the $E(S)$ data. The red curve shows $E(T)$ as determined from the fit with a heat capacity jump ($e = 0$) in Eq. 12. The blue dashed curve shows $E(T)$ as determined from the fit with continuous heat capacity ($e \neq 0$).

with E_0 the ground state energy. For the case with $e \neq 0$, where the heat capacity is continuous, we determine the ordered pairs $[E(S), T(S)]$ as a function of S and plot $E(T)$. Fig. 10 shows the results using the best fits for both cases.

Of particular interest is the low temperature power law. For $e = 0$, we obtain $b = 1.35$ and $b/(b - 1) = 3.86$. Since b is near $4/3$, the energy relative to the ground state scales approximately as T^4 . This is consistent with sound modes dominating the low energy excitations. However, one would expect instead that the free fermions on the edges of the trapped cloud would make an important contribution to the low energy excitations⁸. Over an extended range of $T < T_c$, the net entropy arising from the Bose and Fermi excitations has been predicted to scale as T^2 , yielding an energy scaling⁸ as $E - E_0 \propto T^3$. In this case, one would expect that $E - E_0 \propto S^{3/2}$, i.e., $b = 3/2$ in Eq. 22, so that $b/(b - 1) = 3$. Hence, the low energy power law exponents for the entropy should be between $4/3$ and $3/2$, which is barely distinguishable for our data.

7.2 Heat Capacity versus Temperature

The heat capacity at constant trap depth $C = dE/dT$ is readily obtained from Eq. 22 (where there is a heat capacity jump, since we have constrained $e = 0$ in Eq. 12). For this parameterization,

$$C_{<}(T) = \frac{S_c}{b-1} \left(\frac{T}{T_c} \right)^{\frac{1}{b-1}}; \quad 0 \leq T \leq T_c$$

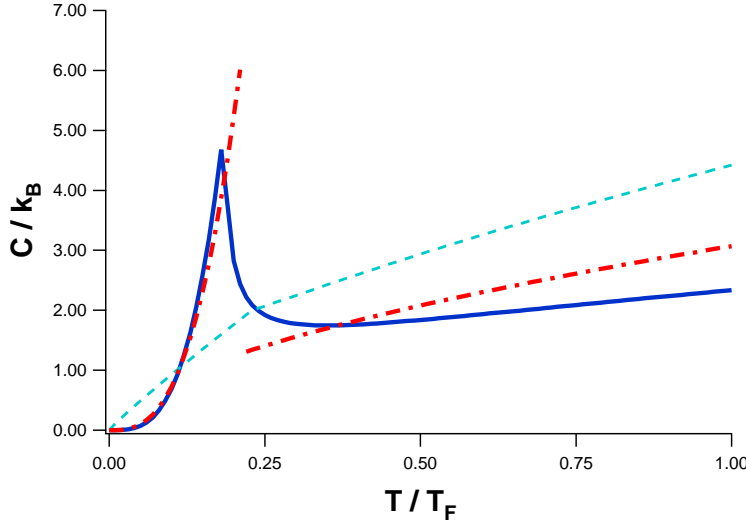


Fig. 11 Color online. Heat capacity versus temperature given by Eq. 24 for a strongly interacting Fermi gas. The red dot-dashed curve shows the heat capacity when there is a jump at $T_c/T_F = 0.21$. The blue solid curve shows the heat capacity when the heat capacity is continuous. For comparison, the light-blue dashed curve shows the heat capacity obtained for an ideal Fermi gas (using the fit function of Fig. 7).

$$C_{>}(T) = \frac{S_c}{d-1} \left(\frac{T}{T_c} \right)^{\frac{1}{d-1}}; \quad T \geq T_c, \quad (24)$$

where T and T_c are given in units of T_F , and S_c is given in units of k_B . For the fit with a continuous heat capacity, we use $T(S)$ to find $C(S) = T(S)/(dT/dS)$, and plot the ordered pairs $[C(S), T(S)]$. The heat capacity curves for both cases are shown in Fig. 11.

According to Eq. 24, a jump in heat capacity occurs at S_c : $C_{<}(T_c) = S_c/(b-1)$ and $C_{>}(T_c) = S_c/(d-1)$ differ when the power law exponents b and d are different. This is a consequence of the simple two power-law structure assumed for the fit function $E(S)$ given by Eq. 12 for $e = 0$, and cannot be taken as proof of a true heat capacity jump. At present, the precise nature of the behavior near the critical temperature cannot be determined from our data, and it remains an open question whether the data exhibits a heat capacity jump or a continuous heat capacity.

7.3 Global Chemical Potential versus Energy

The global chemical potential μ_g is readily determined from the fits to the $E(S)$ data for a strongly interacting Fermi gas, which obeys universal thermodynamics. The local energy density generally takes the form $\varepsilon = T s + \mu n - P$, where ε is the local internal energy, which includes the kinetic energy and the interaction energy. Here, n is the local density, μ is the local chemical potential, P is the pressure and s is the total entropy per unit volume.

The local chemical potential can be written as $\mu = \mu_g - U$, where U is the trap potential. In the universal regime, where the local pressure depends only on the local density and temperature, we have $P = 2\varepsilon/3$, as noted by Ho¹⁵. Hence, $5\varepsilon/3 = Ts + (\mu_g - U)n$. Integrating both sides over the trap volume and using $\int d^3\mathbf{x} \varepsilon = NE - N\langle U \rangle$, where E and $\langle U \rangle$ are the total energy and average potential energy per particle, respectively, we obtain

$$\frac{5}{3}NE - \frac{2}{3}N\langle U \rangle = NTS + \mu_g N, \quad (25)$$

where S is the entropy per particle. For simplicity, we assume harmonic confinement and use the virial theorem result, $\langle U \rangle = E/2$, from Eq. 5, which holds in the universal regime. Then, Eq. 25 yields the global chemical potential of a harmonically trapped Fermi gas in the universal regime,

$$\mu_g = \frac{4}{3}E - TS. \quad (26)$$

By using the fit to the measured entropy-energy data to obtain the temperature $T = \partial E / \partial S$ from Eq. 12, the global chemical potential of a trapped unitary Fermi gas can be calculated from Eq. 26. For $e = 0$, where the heat capacity has a jump, the simple power law fits above and below E_c each yield a different linear dependence of μ_g on E ,

$$\begin{aligned} \mu_g(E) &= \frac{4}{3}E_0 + \left(\frac{4}{3} - b\right)(E - E_0); \quad E_0 \leq E \leq E_c \\ \mu_g(E) &= \mu_g(E_c) + \left(\frac{4}{3} - d\right)(E - E_c); \quad E \geq E_c, \end{aligned} \quad (27)$$

where $\mu_g(E_c) = 4E_0/3 + (4/3 - b)(E_c - E_0)$.

We plot the chemical potential in Fig. 12. The data points are obtained using Eq. 26 with the measured energy E and entropy S and the temperature determined from the fit to the $E(S)$ data, using $e = 0$ in Eq. 12, i.e., with a heat capacity jump. The solid red curve is given by Eq. 27. We note that the low temperature data points in $E(S)$ are best fit with the power law $b = 1.35$, which is close to $4/3$. According to Eq. 27, this produces a slope near zero for $E_0 \leq E \leq E_c$. Since the power-law fit above E_c gives $d = 2.76$, the slope according to Eq. 27 changes from nearly zero for $E_0 \leq E \leq E_c$ to negative for $E \geq E_c$.

Note that from Eq. 26, we obtain the slope

$$\frac{\partial \mu_g}{\partial E} = \frac{1}{3} - \frac{S}{C}. \quad (28)$$

Since the entropy S is continuous, we see that a jump in the heat capacity produces a corresponding jump in the slope of μ_g versus E .

For comparison, Fig. 12 also shows the chemical potential obtained for $e \neq 0$ in Eq. 12, where the heat capacity is continuous (blue dashed curve).

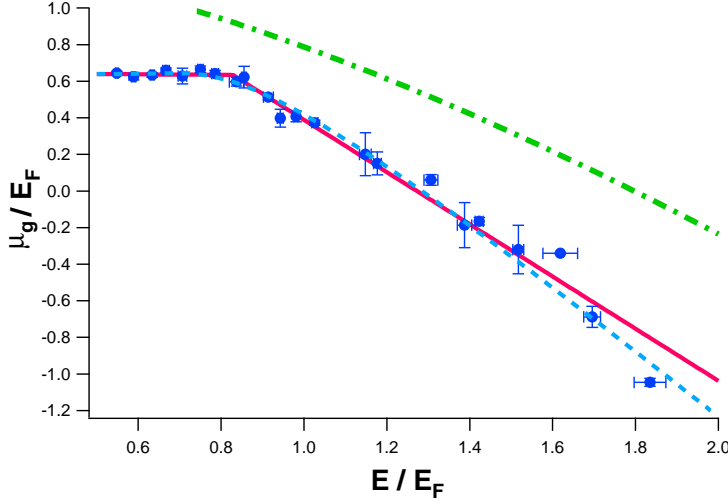


Fig. 12 Color online. The global chemical potential versus the total energy of a strongly interacting Fermi gas. The data points are calculated from the measured $E - S$ data and the fitted T , where T is determined by the fit parameters in Eq. 12 for $e = 0$. The standard deviation for each point of the chemical potential is determined by the standard deviation of the measured $E - S$ data. The solid red lines (heat capacity jump) and blue dashed curve (heat capacity continuous) are determined by the fit parameters used in Eq. 12 according to Eq. 27. The green dot-dashed curve shows the ideal Fermi gas result for the fit function of Fig. ??.

8 Conclusion

We have studied the thermodynamic properties of a strongly interacting Fermi gas by measuring both the energy and the entropy. The model-independent data obtained in both the superfluid and the normal fluid regimes do not employ any specific theoretical calibrations, and therefore can be used as a benchmark to test the predictions from many-body theories and simulations. Parameterizing the energy-entropy data determines the temperature of the strongly interacting Fermi gas and also yields estimates of the critical parameters. We use the measured data to calibrate two different temperature scales that were employed in observations of the onset of pair condensation and in heat capacity studies. These calibrations yield critical temperatures in good agreement with the results estimated from our energy-entropy data. Our data does not determine whether the heat capacity exhibits a jump or is continuous at the critical temperature. However, for a finite system with nonuniform density, the latter is most likely. Considering that there is huge interest in determining the detailed behavior of the superfluid transition in a strongly interacting Fermi gas⁶¹, more precise determinations of the critical temperature, the heat capacity, and the chemical potential near the critical point, as well as the high temperature behavior and the approach to the ideal gas limit, will be important topics for future research.

Acknowledgements

This research has been supported by the Physics divisions of the Army Research Office and the National Science Foundation, the Physics for Exploration program of the National Aeronautics and Space Administration, and the Chemical Sciences, Geosciences and Biosciences Division of the Office of Basic Energy Sciences, Office of Science, U. S. Department of Energy. We thank Willie Ong for a careful reading of the manuscript.

References

1. K. M. O'Hara, S. L. Hemmer, M. E. Gehm, S. R. Granade, J. E. Thomas, *Science* **298**, 2179 (2002).
2. J. E. Thomas, M. E. Gehm, *American Scientist* **92**, 238 (2004).
3. U. Heinz, *Nucl. Phys. A* **721**, 30 (2003).
4. H. Hu, P. D. Drummond, X.-J. Liu, *Nature Physics* **3**, 469 (2007).
5. H. Hu, X.-J. Liu, P. D. Drummond, *Phys. Rev. A* **77**, 061605(R) (2008).
6. R. Haussmann, W. Zwerger, Thermodynamics of a trapped unitary Fermi gas (2008). arXiv:0805.3226.
7. A. Bulgac, J. E. Drut, P. Magierski, *Phys. Rev. Lett.* **99**, 120401 (2007).
8. Q. Chen, J. Stajic, K. Levin, *Phys. Rev. Lett.* **95**, 260405 (2005).
9. J. Kinnunen, M. Rodríguez, P. Törmä, *Science* **305**, 1131 (2004).
10. P. Massignan, G. M. Bruun, H. Smith, *Phys. Rev. A* **71**, 033607 (2005).
11. A. Perali, P. Pieri, L. Pisani, G. C. Strinati, *Phys. Rev. Lett.* **92**, 220404 (2004).
12. M. Houbiers, H. T. C. Stoof, W. I. McAlexander, R. G. Hulet, *Phys. Rev. A* **57**, R1497 (1998).
13. L. Luo, *et al.*, *New Journal of Physics* **8**, 213 (2006).
14. H. Heiselberg, *Phys. Rev. A* **63**, 043606 (2001).
15. T.-L. Ho, *Phys. Rev. Lett.* **92**, 090402 (2004).
16. T. Bourdel, *et al.*, *Phys. Rev. Lett.* **91**, 020402 (2003).
17. J. Kinast, S. L. Hemmer, M. Gehm, A. Turlapov, J. E. Thomas, *Phys. Rev. Lett.* **92**, 150402 (2004).
18. M. Bartenstein, *et al.*, *Phys. Rev. Lett.* **92**, 203201 (2004).
19. J. Kinast, A. Turlapov, J. E. Thomas, *Phys. Rev. Lett.* **94**, 170404 (2005).
20. A. Altmeyer, *et al.*, *Phys. Rev. Lett.* **98**, 040401 (2007).
21. M. J. Wright, *et al.*, *Phys. Rev. Lett.* **99**, 150403 (2007).
22. J. Joseph, *et al.*, *Phys. Rev. Lett.* **98**, 170401 (2007).
23. M. Greiner, C. A. Regal, D. S. Jin, *Nature* **426**, 537 (2003).
24. S. Jochim, *et al.*, *Science* **302**, 2101 (2003).
25. M. W. Zwierlein, *et al.*, *Phys. Rev. Lett.* **91**, 250401 (2003).
26. C. A. Regal, M. Greiner, D. S. Jin, *Phys. Rev. Lett.* **92**, 040403 (2004).
27. M. W. Zwierlein, *et al.*, *Phys. Rev. Lett.* **92**, 120403 (2004).
28. C. Chin, *et al.*, *Science* **305**, 1128 (2004).
29. G. B. Partridge, K. E. Strecker, R. I. Kamar, M. W. Jack, R. G. Hulet, *Phys. Rev. Lett.* **95**, 020404 (2005).
30. C. H. Schunck, Y. il Shin, A. Schirotzek, W. Ketterle, Determination of the fermion pair size in a resonantly interacting superfluid (2008). arXiv:0802.0341.

-
31. J. T. Stewart, J. P. Gaebler, D. S. Jin, *Nature* **454**, 744 (2008).
 32. M. W. Zwierlein, A. Schirotzek, C. H. Schunck, W. Ketterle, *Science* **311**, 492 (2006).
 33. G. B. Partridge, W. Li, R. I. Kamar, Y. Liao, R. G. Hulet, *Science* **311**, 503 (2006).
 34. M. W. Zwierlein, J. R. Abo-Shaeer, A. Schirotzek, C. H. Schunck, W. Ketterle, *Nature* **435**, 1047 (2005).
 35. C. H. Schunck, M. W. Zwierlein, A. Schirotzek, W. Ketterle, *Phys. Rev. Lett.* **98**, 050404 (2007).
 36. B. Clancy, L. Luo, J. E. Thomas, *Phys. Rev. Lett.* **99**, 140401 (2007).
 37. J. Kinast, *et al.*, *Science* **307**, 1296 (2005).
 38. L. Luo, B. Clancy, J. Joseph, J. Kinast, J. E. Thomas, *Phys. Rev. Lett.* **98**, 080402 (2007).
 39. Q. Chen, C. Regal, M. Greiner, D. Jin, K. Levin, *Phys. Rev. A* **73**, 041601(R) (2006).
 40. M. Zwierlein, C. Schunck, A. Schirotzek, W. Ketterle, *Nature* **442**, 54 (2006).
 41. M. Bartenstein, *et al.*, *Phys. Rev. Lett.* **94**, 103201 (2005).
 42. J. E. Thomas, J. Kinast, A. Turlapov, *Phys. Rev. Lett.* **95**, 120402 (2005).
 43. F. Werner, Y. Castin, *Phys. Rev. A* **74**, 053604 (2006).
 44. D.T.Son, *Phys. Rev. Lett.* **98**, 020604 (2007).
 45. F. Werner, Virial theorems for trapped quantum gases (2008). arXiv:0803.3277[cond-mat.other].
 46. J. E. Thomas, *Phys. Rev. A* **78**, 013630 (2008).
 47. L. Luo, Entropy and superfluid critical parameters of a strongly interacting Fermi gas, Ph.D. thesis, Duke University (2008).
 48. J. T. Stewart, J. P. Gaebler, C. A. Regal, D. S. Jin, *Phys. Rev. Lett.* **97**, 220406 (2006).
 49. Q. Chen, pseudogap theory of a trapped Fermi gas, private communication.
 50. A. Bulgac, J. E. Drut, P. Magierski, *Phys. Rev. Lett.* **96**, 090404 (2006).
 51. E. Burovski, E. Kozik, N. Prokof'ev, B. Svistunov, M. Troyer, *Phys. Rev. Lett.* **101**, 090402 (2008).
 52. G. F. Bertsch proposed the problem of determining the ground state of a two-component Fermi gas with a long scattering length and defined the parameter ξ .
 53. G. A. Baker, Jr., *Phys. Rev. C* **60**, 054311 (1999).
 54. H. Heiselberg, *Phys. Rev. A* **63**, 043606 (2001).
 55. J. Carlson, S.-Y. Chang, V. R. Pandharipande, K. E. Schmidt, *Phys. Rev. Lett.* **91**, 050401 (2003).
 56. M. E. Gehm, S. L. Hemmer, S. R. Granade, K. M. O'Hara, J. E. Thomas, *Phys. Rev. A* **68**, 011401(R) (2003).
 57. C. Chin, *Phys. Rev. A* **72**, 041601(R) (2005).
 58. S. Y. Chang, V. R. Pandharipande, J. Carlson, K. E. Schmidt, *Phys. Rev. A* **70**, 043602 (2004).
 59. G. E. Astrakharchik, J. Boronat, J. Casulleras, S. Giorgini, *Phys. Rev. Lett* **93**, 200404 (2004).
 60. J. Carlson, S. Reddy, *Phys. Rev. Lett.* **100**, 150403 (2008).
 61. R. Haussmann, W. Rantner, S. Cerrito, W. Zwerger, *Phys. Rev. A* **75**, 023610 (2007).